

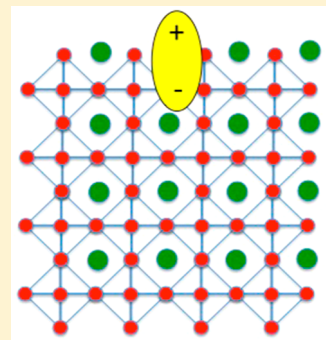
Trap States in Lead Iodide Perovskites

Xiaoxi Wu,[†] M. Tuan Trinh,[†] Daniel Niesner,[†] Haiming Zhu,[†] Zachariah Norman, Jonathan S. Owen, Omer Yaffe, Bryan J. Kudisch, and X.-Y. Zhu*

Department of Chemistry, Columbia University, New York, New York 10027, United States

Supporting Information

ABSTRACT: Recent discoveries of highly efficient solar cells based on lead iodide perovskites have led to a surge in research activity on understanding photo carrier generation in these materials, but little is known about trap states that may be detrimental to solar cell performance. Here we provide direct evidence for hole traps on the surfaces of three-dimensional (3D) $\text{CH}_3\text{NH}_3\text{PbI}_3$ perovskite thin films and excitonic traps below the optical gaps in these materials. The excitonic traps possess weak optical transition strengths, can be populated from the relaxation of above gap excitations, and become more significant as dimensionality decreases from 3D $\text{CH}_3\text{NH}_3\text{PbI}_3$ to two-dimensional (2D) $(\text{C}_4\text{H}_9\text{NH}_3)_2(\text{CH}_3\text{NH}_3\text{I})_{n-1}(\text{PbI}_2)_n$ ($n = 1, 2, 3$) perovskites and, within the 2D family, as n decreases from 3 to 1. We also show that the density of excitonic traps in $\text{CH}_3\text{NH}_3\text{PbI}_3$ perovskite thin films grown in the presence of chloride is at least one-order of magnitude lower than that grown in the absence of chloride, thus explaining a widely known mystery on the much better solar cell performance of the former. The trap states are likely caused by electron–phonon coupling and are enhanced at surfaces/interfaces where the perovskite crystal structure is most susceptible to deformation.

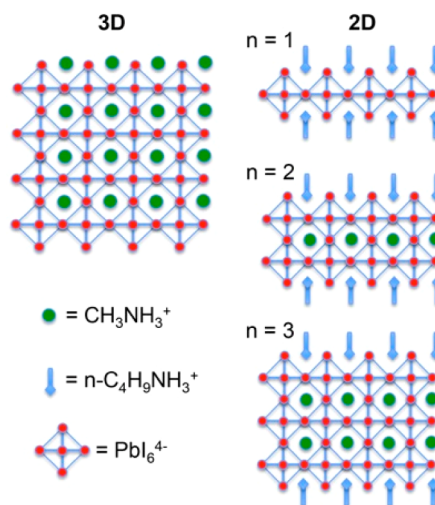


1. INTRODUCTION

Lead halide perovskites are emerging as one of the most promising classes of materials for low-cost photovoltaic technology.^{1–9} Intense research efforts on these materials are underway to establish the fundamental photophysical mechanisms,^{10–14} to improve chemical stability,¹⁵ environmental compatibility,¹⁶ and process reproducibility.^{7,17} In addition to the three-dimensional (3D) crystalline form used in recent solar cell studies, lead halide perovskites can also be prepared in two-dimensional (2D) crystalline forms that are natural quantum wells.^{18–20} Both 3D and 2D lead iodide perovskites share the same PbI_6 octahedral building blocks (Scheme 1). In the 2D form,¹⁸ the inorganic layer can consist of one ($n = 1$), two ($n = 2$) or three ($n = 3$) lead iodide octahedral layers, charge balanced on each of the two surfaces by organic cations, e.g., $2 \times \text{C}_4\text{H}_9\text{NH}_3^+$.

Recent photophysical studies concluded that the initial optical excitation in $\text{CH}_3\text{NH}_3\text{PbI}_3$ perovskites is excitonic in nature, but the low exciton binding energy ensures its prompt and near complete dissociation into charge carriers with long electron/hole diffusion lengths.^{14,21,22} One critical factor detrimental to solar cell performance is charge carrier trapping, which introduces competitive recombination channels.^{23,24} The charge carrier trap density is necessarily low for a highly efficient solar cell, but traps can be formed at interfaces with electron or hole extraction layers^{23,25} or increase with time due to chemical/structural changes to the material. It is also known that solar cell efficiency is very sensitive to material synthesis and processing conditions. As a prominent example, the $\text{CH}_3\text{NH}_3\text{PbI}_3$ perovskite made from PbCl_2 precursor is similar to that from PbI_2 in terms of crystal structure, chemical

Scheme 1. Schematic Structures of the 3D and 2D Organo-Lead Halide Perovskites Used in the Present Study



composition, and photophysical properties,^{26,27} but solar cells made with the former show higher efficiencies than those from the latter.^{12,28,29} In the literature, the sample grown from PbCl_2 has been called mixed halide perovskite (with a molecular formula of $\text{CH}_3\text{NH}_3\text{PbI}_{3-x}\text{Cl}_x$), but a consensus arising from most recent experiments is that both $\text{CH}_3\text{NH}_3\text{PbI}_3$ and $\text{CH}_3\text{NH}_3\text{PbI}_{3-x}\text{Cl}_x$ seem to possess the same structure and

Received: December 20, 2014

stoichiometry.²⁶ In the following, we will use $\text{CH}_3\text{NH}_3\text{PbI}_3$ to represent 3D perovskites from both PbCl_2 and PbI_2 precursors. The exact difference between the two sample preparations is not fully understood, but one reason might be a higher density of trap states in $\text{CH}_3\text{NH}_3\text{PbI}_3$ perovskites from PbI_2 than that from PbCl_2 .

Most of the published literature on the photophysics of perovskites focused on excitons in 2D crystals^{20,30,31} or carrier generation in 3D crystals.^{10–14,21,22} There is very little knowledge on the physical nature of trap states^{23,32,33} or strategies to control or minimize them.³⁴ Here we provide direct experimental probe of charge and exciton traps in both 3D and 2D lead iodide perovskites. We suggest that these trap states result from electron–phonon coupling and are stabilized at surfaces/interfaces of perovskite crystallites.

2. EXPERIMENTAL SECTION

Preparation of 2D Perovskites. We followed the liquid phase crystallization method reported before¹⁸ to produce the layered lead(II) iodide crystals. Lead(II) iodide (99%), hydriodic acid (57 wt %, stabilizer free in water), *n*-butylamine (99.5%), and methylamine solution (33 wt % in ethanol) were purchased from Sigma-Aldrich and diethyl ether (BHT stabilized) was purchased from Fisher Scientific. All reagents were used without further purification. A minimum volume of hydriodic acid was used to dissolve stoichiometric quantities of lead(II) iodide, *n*-butylamine, and methylammonium iodide at 110 °C. To obtain the crystals, we slowly (~ 2 °C/h) cooled the solution to -10 °C. After cooling, plate-like bright-colored crystals with a few mm^2 areas were obtained. These crystals were then filtered in cold diethyl ether and dried at 60 °C under vacuum for 24 h before exfoliation. The crystals were mechanical exfoliated and transferred onto isopropanol rinsed sapphire crystal (*z*-cut, 0001 orientation, MTI cooperation) for TA and PL measurements or fused silica for linear absorption measurements.

Preparation of 3D Perovskites from Vapor Deposition. We followed the method of Liu et al. using dual-source thermal evaporation method to prepare $\text{CH}_3\text{NH}_3\text{PbI}_3$ perovskite thin films.⁷ $\text{CH}_3\text{NH}_3\text{I}$ powders were synthesized from hydriodic acid (57 wt %, stabilizer free in water, Sigma-Aldrich) and methylamine solution (33 wt % in ethanol, Sigma-Aldrich). PbI_2 and PbCl_2 were purchased from Sigma-Aldrich and used as received. Sapphire crystals (*z*-cut, 0001 orientation, MTI cooperation), silica plates, or native oxide terminated silicon wafers (highly doped, 111 orientation), were used as substrates and rinsed with isopropanol prior to use. For the preparation of so-called mixed halide perovskites, we evaporated $\text{CH}_3\text{NH}_3\text{I}$ and PbCl_2 from separate crucibles in a high vacuum chamber (base pressure $<10^{-7}$ mbar) with the ratio of deposition rates of $\sim 10:1$, as monitored by a quartz crystal microbalance (QCM) positioned next to the sample substrates. For the preparation of pure lead iodide perovskite, we evaporated $\text{CH}_3\text{NH}_3\text{I}$ and PbI_2 from separate crucibles with the ratio of deposition rates of $\sim 4:1$. During the vapor-deposition process, the substrates were slowly rotated along the surface normal for homogeneous film formation. The vapor pressure (mainly due to $\text{CH}_3\text{NH}_3\text{I}$) was $\sim 2 \times 10^{-5}$ Torr during deposition. The obtained perovskite films were annealed in the vacuum chamber in methylammonium iodide atmosphere (2×10^{-5} mbar) or transferred into a N_2 filled glovebox and annealed at 100 °C for 40 min to remove the excess organic molecules and to facilitate further crystallization. Figure S1 shows photos of two typical $\text{CH}_3\text{NH}_3\text{PbI}_3$ perovskite thin film samples on sapphire substrates.

Transient Absorption (TA) Measurement. All samples were mounted in a N_2 filled sample cell for TA measurements at room temperature. In brief, the beam from a Ti:sapphire femtosecond regenerative amplifier at 800 nm wavelength and 1 kHz repetition rate was split into two paths. The first path was directed into an optical parametric amplifier to generate tunable pump laser (UV to near IR). The second path was focused onto a sapphire crystal to produce the white-light supercontinuum (visible: 450–830 nm, NIR: 850–1600

nm) as probe. The pump beam was lightly focused to 0.7 mm^2 at 350 nm pump or 3.3 mm^2 at 420 nm pump and the probe beam to 0.09 mm^2 ; the probe spot was located within the pump spot on the sample surface. The transmitted probe beam was focused onto a fiber coupled high-speed multichannel detector and collected by a high speed spectrometer (HELIOS, Ultrafast Systems).

Room Temperature Absorption and Photoluminescence (PL) Measurement. We recorded linear absorption spectra of 2D perovskites on a LAMBDA 950 UV–vis–NIR Spectrophotometer (PerkinElmer) with an integrating sphere. In order to reduce scattering background, we used a 10 cm focal lens to lightly focus the white light onto the exfoliated 2D perovskites flakes. The transmitted light was collected by an integrating sphere with the correction of substrate absorption. We recorded the linear absorption spectra of 3D perovskite samples on a Shimadzu UV-1800 spectrophotometer without the use of an integrating sphere.

We used a Raman microscope (Renishaw InVia) in the photoluminescence (PL) mode for the room temperature PL measurements on 2D perovskites. For $n = 1$ 2D perovskites, 405 nm CW pump laser was focused by a 10 \times objective and PL in the reflective direction was collected; while for $n = 2$ and $n = 3$ 2D perovskites, a 532 nm CW pump laser source and a 5 \times objective were used. The samples were mounted in a N_2 filled sample cell and no photo damage was observed in all measurements.

Temperature Dependent Fluorescence Measurement. For temperature dependent fluorescence measurement, samples (2D $n = 1$ sample and 3D lead iodide perovskites) on silica substrates were mounted in a cryostat (Janis ST-100) and cooled by liquid nitrogen. The samples were excited by 402 nm light generated by the doubled output of a regenerative amplifier (Coherent Mira seeded RegA, 250 kHz, ~ 100 fs). The excitation density on the sample was kept below $1 \mu\text{J}/\text{cm}^2$ per pulse. The fluorescence from each sample was collected by a liquid nitrogen cooled spectrometer (PyLON 400 with SP-2300 spectrograph, Princeton Instruments).

Ultraviolet Photoelectron Spectroscopy (UPS) Measurements. We carried out UPS measurement in an ultrahigh vacuum (UHV) chamber with a base pressure $<10^{-11}$ Torr using a Phoibos-100 electron analyzer (Specs GMBH) equipped with a delay line detector for electron counting. The energy resolution was set to 100 meV. Spectra were integrated over detection angles of $\pm 7^\circ$ around normal emission. We used two UV sources. In the first set of experiment, a helium gas discharge lamp with photon energy of 21.2 eV served as a UV source. In the second set of experiments, we used a UV laser light source. It consisted of a femtosecond fiber optical amplifier operating at $1.03 \mu\text{m}$, 250 fs pulse width, 1 MHz repetition rate, and 10W power (Clark, Impluse) pumping a homemade noncollinear optical parametric amplifier (NOPA) operating in the near-IR region. The NOPA output was frequency quadrupled to give UV light at $h\nu = 5.79$ eV, with pulse width ~ 100 fs and average power of $\sim 0.3 \mu\text{W}$ on the sample surface. The UV light was directed on the sample surface at 45° from surface normal to give a laser spot of $\sim 1 \text{ mm}^2$. The sample temperature was held at 200 K during UPS measurement. We used $\text{NH}_3\text{CH}_3\text{PbI}_3$ perovskites thin films vapor deposited in a UHV chamber connected to the UHV analysis chamber. The perovskite thin films, on native SiO_2 terminated Si(111), were annealed in situ in methylammonium iodide atmosphere (2×10^{-5} mBar) at 400 K for 15 min before UPS measurement. The same samples were also transferred out the vacuum and characterized by UV–vis spectroscopy and X-ray diffraction.

3. RESULTS AND DISCUSSION

Charge Carrier Traps on the Surface of 3D Perovskites. The first evidence of trap states comes from ultraviolet photoemission spectroscopy (UPS). UPS is a surface sensitive technique and, thus, is particularly suited for probing the preferential trapping of charge carriers on perovskites surfaces. We prepared thin film samples (~ 30 nm thickness, see Supporting Information, Figure S1 for optical images) on native oxide terminated silicon using vapor phase deposition in

high vacuum from $\text{CH}_3\text{NH}_3\text{I}$ and PbI_2 or PbCl_2 precursors (7). X-ray diffraction analysis (Supporting Information, Figure S2) confirmed the excellent crystalline quality of 3D $\text{CH}_3\text{NH}_3\text{I}$ perovskites and UV–vis absorption spectra (see Figure 2A below) were in agreement with published spectra. We show in Figure 1A UPS spectra obtained with He–I UV source ($h\nu =$

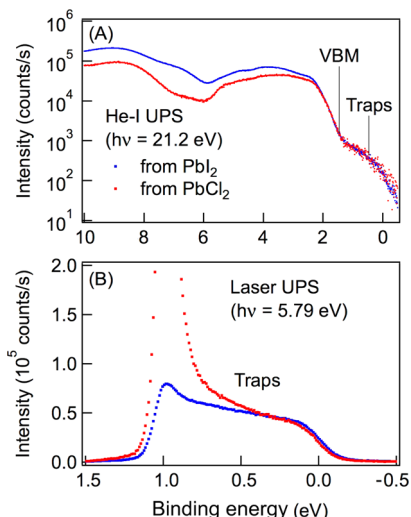


Figure 1. (A) Ultraviolet photoemission spectra obtained with $h\nu = 21.2$ eV (He–I) for $\text{CH}_3\text{NH}_3\text{PbI}_3$ thin films vapor deposited on native oxide terminated silicon from PbI_2 (blue) and PbCl_2 (red) precursors. (B) Ultraviolet photoemission spectrum obtained with $h\nu = 5.79$ eV (laser) of $\text{CH}_3\text{NH}_3\text{PbI}_3$ thin films grown from PbI_2 (blue) and PbCl_2 (red). The binding energy scale is referenced to the Fermi level.

21.2 eV) for the two 3D perovskite thin film samples obtained from PbI_2 (blue) and PbCl_2 (red) precursors. Here, the binding

energy (BE) is referenced to the Fermi level. The two spectra are similar, both showing the valence band maxima (VBM) at $\text{BE} = 1.4$ eV, in agreement with recent work of Schultz et al.³⁵ On the semilogarithmic scale, we can clearly see additional density of states above the VBM, extending to the Fermi level. We assign these midgap states, with density approximately 2 orders of magnitude lower than that of the valence band, to charge carrier (hole) traps.

To better resolve the trap states above the VBM, we use a laser based UV source with $h\nu = 5.79$ eV. This lower photon energy enhances the ionization cross section for the trap states by almost 3 orders of magnitude as compared to that from the He–I source. We can now clearly see the trap states extending to the Fermi level in Figure 1B. The sharp peak at $\text{BE} \geq 1$ eV is near the threshold (zero) kinetic energy of emitted photoelectrons and originates both from the high energy tail of the valence band and secondary electrons. The difference in the intensities of the threshold peak from the two sample preparations can be attributed to small variations in work-function.

The UPS results in Figure 1 establish the presence of a broad distribution of hole traps on the surfaces of the $\text{CH}_3\text{NH}_3\text{PbI}_3$ perovskite thin films. Although not detectable by UPS, we expect similarly trapped electrons below the conduction band minimum. Supporting this, we show below the presence of excitonic traps: both an electron and a hole trapped locally with nonzero optical transition strength. Surprisingly, while the two sample preparations (from PbI_2 and PbCl_2 precursors) are known to give very different solar cell efficiencies, the trap state densities from UPS measurements are similar. Since UPS is only surface sensitive, the results in Figure 1 suggest that perovskite thin films from PbI_2 and PbCl_2 give similarly exposed surfaces. We believe the different solar cell efficiencies of perovskites grown from PbI_2 and PbCl_2 likely come from

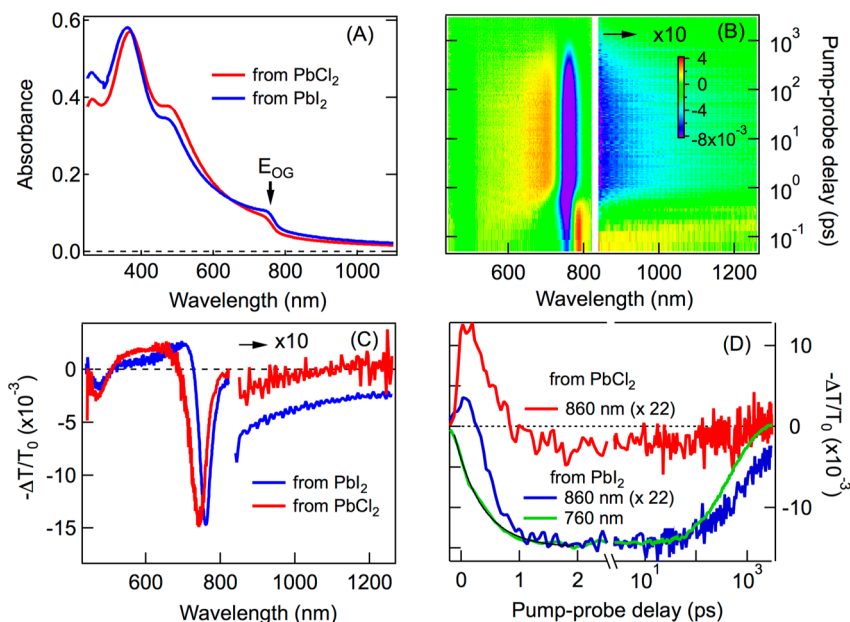


Figure 2. (A) Static absorption spectra of perovskites prepared from PbI_2 and PbCl_2 . (B) Two-dimensional pseudocolor $(-\Delta T/T_0)$ plots of TA spectra as functions of probe wavelength and pump–probe delay (Δt) for the perovskite grown from PbI_2 precursor. The $-\Delta T/T_0$ values above 840 nm are multiplied by a factor of 10. Pump: 420 nm, ~ 100 fs pulse width, $6.4 \mu\text{J}/\text{cm}^2$ pulse energy density. Probe: white light super continuum, ~ 200 fs pulse width, $\leq 0.1 \mu\text{J}/\text{cm}^2$ pulse energy density. (C) TA spectra at $\Delta t = 2$ ps for the sample prepared from PbI_2 (blue) and PbCl_2 (red). (D) Kinetic profiles at probe wavelengths of 860 nm ($\times 22$) for the sample from PbI_2 (blue) and PbCl_2 (red) and 760 nm for the sample from PbI_2 (green).

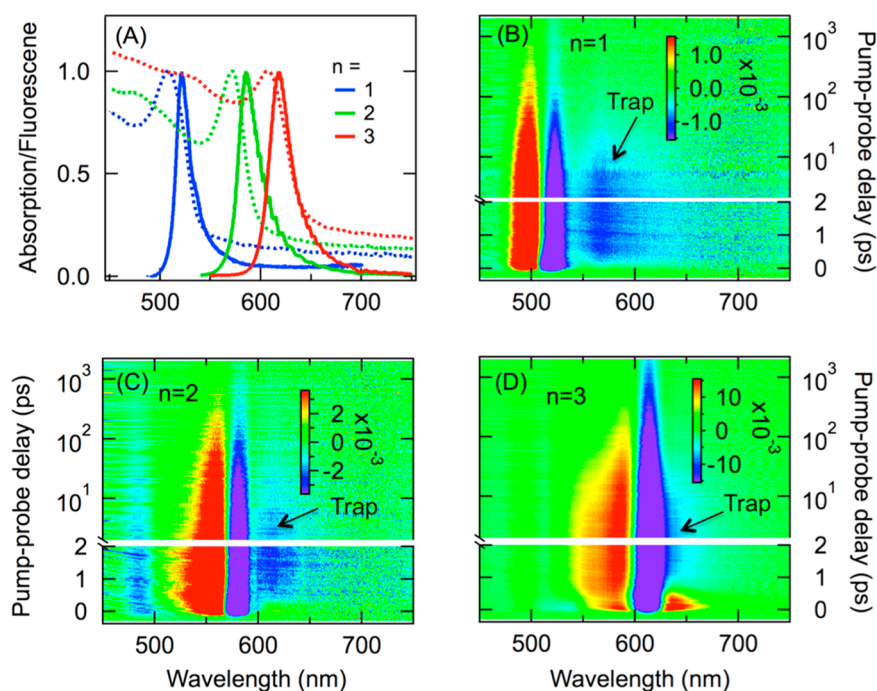


Figure 3. Two-dimensional pseudocolor ($-\Delta T/T_0$) plots of TA spectra as functions of probe wavelength and pump–probe delay (Δt) for 2D perovskite thin film samples, $(\text{C}_4\text{H}_9\text{NH}_3\text{I})_2(\text{CH}_3\text{NH}_3\text{I})_{n-1}(\text{PbI}_2)_n$: (B) $n = 1$; (C) $n = 2$; (D) $n = 3$. The arrows in panels B–C point to trap states. Panel (A) shows static absorption (dotted) and fluorescence spectra (solid) of the three 2D perovskite samples (blue, green, red for $n = 1, 2, 3$, respectively).

difference in the bulk, e.g., boundaries and interfaces between crystallites, as we show below with bulk sensitive optical spectroscopies.

Excitonic Traps in 3D Perovskites. Optical absorption spectra (Figure 2A) of the 3D perovskite thin films (on sapphire) showed the optical gap (the first exciton transition, marked by an arrow) at 760 ± 5 nm ($E_{\text{OG}} = 1.63 \pm 0.01$ eV) and 750 ± 5 nm (1.65 ± 0.01 eV) for samples from the PbI_2 and PbCl_2 precursors, respectively, in agreement with previous reports.^{3,10,14} However, the possible presence of trap states below E_{OG} cannot be judged from these static absorption spectra due to unavoidable presence of scattering. We use transient absorption (TA) spectroscopy to probe the trap states. Each perovskite sample is photoexcited by a pump laser pulse above the bandgap at 420 nm and probed at a controlled delay time by a probe pulse of white light continuum. Figure 2B shows a pseudocolor representation of TA spectrum ($-\Delta T/T_0$) as functions of probe wavelength and pump–probe delay time for the $\text{CH}_3\text{NH}_3\text{PbI}_3$ sample grown from PbI_2 . ΔT is the change in transmission with the pump pulse and T_0 is the transmission without pump pulse. The main feature in a broad time window ($\Delta t = 1$ ps to 3 ns) is ground-state bleaching (GB) at the optical gap around 760 nm, attributed to state-filling, i.e., the presence of band gap carriers or excitons from the pump pulse blocking optical transition induced by the probe pulse. At shorter times ($\Delta t < 1$ ps), we observe a derivative spectral profile around 760 nm, assigned to a red-shift of the band gap transition in the presence of hot carriers. Figure 2D shows $-\Delta T/T_0$ probed at 760 nm for the band-edge excitons (green), with growth in GB due to hot carrier cooling well described by a single exponential lifetime of $\tau = 0.5 \pm 0.1$ ps (black curve). The nanosecond decay time is shorter than those reported before^{10–12} and can be attributed to Auger recombination at the high pump-power density ($6.4 \mu\text{J}/\text{cm}^2$,

see Supporting Information, Figure S3A and S3B, for dependence on pump power). The high pump intensity is chosen to clearly show the trap states with low absorption cross sections.

Concurrent with the cooling of hot carriers, TA spectra in Figure 2B show the appearance of a weak but clearly observable bleach signal below E_{OG} (note that the $-\Delta T/T_0$ signal in Figure 2B is multiplied by a factor of 10 for probe wavelength ≥ 840 nm). Horizontal cuts for $\Delta t > 1$ ps (blue curve in Figure 2C for $\Delta t = 2$ ps) reveal the main bleach signal at 760 nm (E_{OG}), and a broad and weak bleach feature below the optical gap. The bleaching in the near-infrared reveals the excitonic nature of the traps: they process weak optical transition strength in the ground state and are populated from the relaxation of hot carriers, resulting in the blocking of the weakly allowed transitions during the probe pulse. These excitonic traps are characterized by a broad distribution decaying away from E_{OG} . The trap state formation time increases with excitation photon energy (Supporting Information, Figure S3D), as is expected from the transfer of excess carrier energy to phonons.

We now compare the two 3D $\text{CH}_3\text{NH}_3\text{PbI}_3$ perovskite thin films grown from PbI_2 and PbCl_2 precursors, with the latter known to give higher solar cell efficiency.^{10,12} Figure 2C shows TA spectra at $\Delta t = 2$ ps for $\text{CH}_3\text{NH}_3\text{PbI}_3$ from PbI_2 (blue) and PbCl_2 (red) precursors. For the sample grown from PbCl_2 , the magnitude of bleaching attributed to traps is at least 1 order of magnitude lower than that grown from PbI_2 . The difference is evident throughout the time window in Figure 2D, which compares $-\Delta T/T_0$ probed at 860 nm. At this probe wavelength, the $-\Delta T/T_0$ signal at $\Delta t \leq 1$ ps contains excited state absorption of hot carriers as well as GB of below-gap states; at $\Delta t > 1$ ps, GB of trap states dominates. The much lower density of trap states in the 3D $\text{CH}_3\text{NH}_3\text{PbI}_3$ perovskite

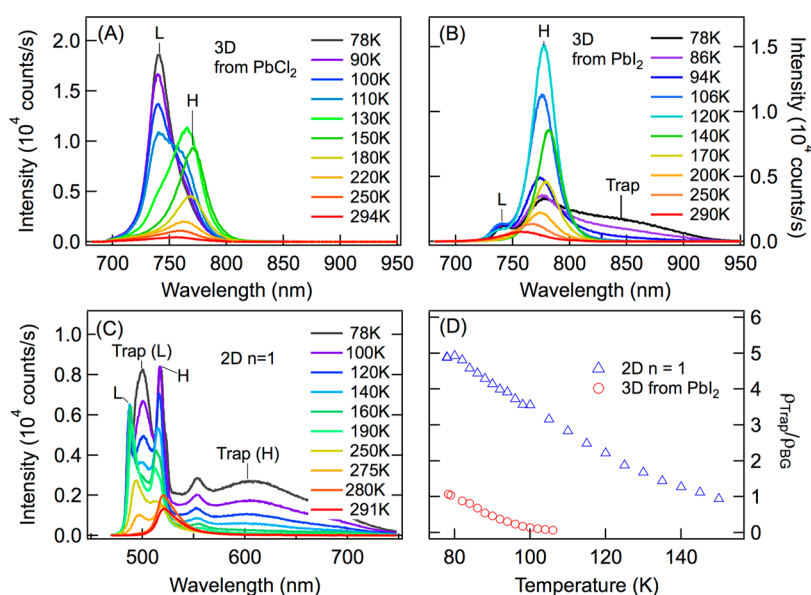


Figure 4. Temperature dependent fluorescence spectra from (A) 3D lead iodide perovskite thin film from PbCl_2 precursor; (B) 3D lead iodide perovskite thin film from PbI_2 precursor; (C) 2D $n = 1$ lead iodide perovskite, $(\text{C}_4\text{H}_9\text{NH}_3)_2(\text{PbI}_2)$. (D) Ratio between PL emission from below-gap traps and that from band gap excitons as a function of temperature for 2D $n = 1$ perovskite (triangle) and 3D perovskites from PbI_2 .

grown from PbCl_2 than that from PbI_2 correlates with the slower decay (2.6 ns) of band gap excitation in the former than that (0.8 ns) in the latter (Supporting Information, Figure S3C). Compared to the band-edge excitons, the trapped excitons possess higher binding energies and, thus, a lower probability of dissociation into charge carriers and a higher probability of recombination.¹² While we focus on 3D perovskites obtained from vapor deposition, we also observe similar below-gap trap states in solution processed $\text{CH}_3\text{NH}_3\text{PbI}_3$ perovskite (Supporting Information, Figure S4).

Our observation of much lower trap state density in $\text{CH}_3\text{NH}_3\text{PbI}_3$ perovskite from PbCl_2 than that from PbI_2 is consistent not only with the better solar cell performance in the former,^{12,28,29} but also with the different film morphologies observed in structural characterizations.^{27,36,37} Recent experiments have revealed the same crystalline structure and chemical composition of $\text{CH}_3\text{NH}_3\text{PbI}_3$ perovskites from both PbCl_2 and PbI_2 precursors, but different film morphology and crystallite size/shape from the two preparations. The presence of chloride ions during growth has been shown to result in large and elongated crystallites with μm dimensions, while that in the absence of chloride shows much smaller crystallites with 10^2 nm dimensions.^{27,36,37} Since smaller crystallites means larger interfacial area, we hypothesize that the trap states are located at the crystallite surfaces/interface and this can explain the higher density of trap states in the thin film from PbI_2 than that from PbCl_2 . The smaller crystals grown in the absence of chloride ions lack well-defined facets and are randomly packed;^{27,36} the interfaces between these poorly defined crystallites are likely the locations of trap states. In contrast, the larger crystals grown in the presence of chloride ions feature well-defined facets of low Miller indices²⁷ and coherent long-range packing of the crystals in the film.³⁶ A DFT calculation by Haruyama et al. suggested negligible trapping on low-index crystalline faces of the tetragonal perovskite crystal.³⁸ Close interaction between the well-defined facets of neighboring crystals in coherently packed film can also effectively heal the

trap states. In the following, we provide further evidence for the surface/interface interpretation of trap states.

Excitonic Traps in 2D Perovskites. The excitonic traps discovered above for the 3D perovskites are much enhanced in the quantum-confined 2D perovskites. Figure 3A shows room temperature absorption and PL spectra of the three 2D perovskite samples ($n = 1, 2, 3$). As the quantum well thickness increases from $n = 1$ to $n = 2$ and $n = 3$, the 1S exciton transition shifts from 508 to 571 and 608 nm, respectively. The corresponding PL peaks are at 521, 587, and 619 nm, for $n = 1, 2$, and 3, respectively. Interestingly, each PL spectrum is characterized by an asymmetric line-shape, tailing to longer wavelength. As we show below, the lower energy PL tail comes from radiative recombination of trap states.

Figure 3B–D shows pseudocolor representations of TA spectra obtained from 2D perovskites with $n = 1, 2$, and 3, respectively. In each case, the sample is excited above the band gap at 350 nm and probed by a white light continuum. A detailed analysis of the linear power dependence is shown in Supporting Information (Figures S5 and S6). We observe two common features in all three samples. The first is a blue-shift in the band-edge (1S) exciton energy, resulting in a derivative feature with bleaching at or below the exciton transition and induced absorption above. This is particularly evident for $n = 1$ and 2 samples, where the positive signal and the negative signal can be well described by blue-shifts of ~ 4 nm (Supporting Information, Figures S7 and S8). The second common feature is the broad and weak bleaching below the optical gap; similar to the situation for the 3D sample in Figure 2, the observation of bleaching reveals that these trap states are excitonic in nature since they possess optical transition strength and the direct optical transition of these trap states can be blocked during the probe pulse by those formed indirectly from the relaxation of hot carriers/excitons.

The transient absorption spectra in Figure 3 show that the density of excitonic traps increases with quantum confinement. The relative magnitudes of peak bleaching signal from the trap states (normalized to the peak of the blue-shifted bleaching

signal of the band-edge 1S exciton) are $\gamma = 0.077, 0.25$, and 0.30 for $n = 3, 2$, and 1 , respectively (Supporting Information, section 4.3 and Figure S9). For comparison, we obtain $\gamma = 0.045$ for 3D perovskite from the PbI_2 precursor in Figure 2. The increase in trap density is correlated with the relative area of the organic/inorganic interface, each consisting of a soft butylamine organic layer on a hard inorganic lead iodide quantum well. Such an interface is similar to an exposed surface of a 3D perovskite crystal, consisting of a methylamine organic layer on the inorganic lead iodide crystal. Note that the presence of the blue-shift of the band-gap exciton may be attributed to the band-gap renormalization resulting from the exciton-exciton interactions in quantum confined two-dimensional quantum wells (Supporting Information, section 4.2).

Fluorescence Emission from Excitonic Traps. Further evidence for the excitonic traps comes from temperature dependent fluorescence emission. Figure 4 shows a set of fluorescence spectra at different temperatures (room to liquid nitrogen) with excitation at 402 nm for three perovskite samples: (A) 3D perovskite grown from PbCl_2 ; (B) 3D perovskite grown from PbI_2 ; and (C) 2D perovskite ($n = 1$). For 3D perovskite grown from PbCl_2 (Figure 4A), the sample shows weak fluorescence (peak at ~ 754 nm) at room temperature. The fluorescence intensity increases by more than an order of magnitude as temperature decreases to ~ 180 K and this is accompanied by a red-shift in the peak position to ~ 768 nm. At $T \leq 150$ K, a new fluorescence peak emerges at 741 nm; this blue-shifted peak further grows with decreasing T and becomes the dominant feature at the lowest temperature probed here $T = 78$ K. The evolution of fluorescence spectra in 3D lead iodide perovskite with decreasing temperature can be attributed to a tetragonal-to-orthorhombic phase transition, as revealed by previous optical absorption measurement.¹⁴ The room temperature tetragonal phase (denoted as H phase), which gives the fluorescence peak at 754–768 nm, corresponds to the collective rotation (around the c -axis) of each PbI_6 octahedron from its symmetric position in the simple cubic structure, while the low temperature (L) phase, with fluorescence peak at ~ 741 nm, corresponds to the tilting of the PbI_6 octahedra out of the ab plane.^{14,39,40}

For 3D perovskite from PbI_2 (Figure 4B), the phase transition process is similar to that from PbCl_2 : fluorescence from the H phase peaks at 759 nm at room temperature and red-shifts gradually to 782 nm as T decreases to 140 K. Below that, the L phase appears in the blue region. The H phase emission is still intense even at 78 K. The incomplete phase transition has also been observed previously in lead iodide perovskite by Wehrenfennig et al., which presumably can be explained by the strain effect imposed by the phase transition.⁴⁰ The presence of the H phase at low temperatures is obscured in optical absorption spectra¹⁴ but is dominant in fluorescence spectra in Figure 4B. The latter can be attributed to the efficient excitonic energy transfer from the high-energy L phase to the low-energy H phase. The most important result from Figure 4B is the clear growth of below gap fluorescence with decreasing temperature. At 78 K, the integrated fluorescence intensity from these trap states in the broad wavelength range of 800–950 nm is equal to the total band gap fluorescence from the two phases (H and L). The observation of trap state fluorescence in 3D perovskites from the PbI_2 precursor, but not in that from PbCl_2 , is in perfect agreement with transient absorption results in Figure 2, which shows measurable optical transition strength for the trap states in the former, but not in the latter.

As we concluded earlier, the excitonic traps observed in 3D perovskites are much enhanced in the quantum-confined 2D perovskites. This trend is confirmed in fluorescence spectra, as shown for the $n = 1$ 2D perovskite sample in Figure 4C. At room temperature, the $n = 1$ 2D perovskite exists as a single phase (H) with the fluorescence peak at 521 nm. As T decreases (≤ 280 K), we see the appearance of the L phase¹⁸ with fluorescence peak at ~ 496 nm and blue-shifting to ~ 488 nm at 78 K. Concurrent with the evolution of sharp band gap transitions of both H and L phases is the growth of below-gap fluorescence: a relatively broad peak around 500 nm and another broader emission ranging from ~ 550 to 750 nm. The ~ 500 nm emission can be assigned to traps associated with the L phase while the broad peak 550–750 nm to traps associated with both phases. The assignment of the ~ 560 nm peak on top of the broad emission is unclear, but multiple below gap emission peaks have been observed previously in 2D lead perovskite samples.³⁰

Figure 4D plots the ratio, $\rho_{\text{trap}}/\rho_{\text{BG}}$, of integrated trap state emission to integrated band gap (BG) emission (from both H and L phases) for the 2D ($n = 1$) and 3D (from PbI_2) perovskites (see Supporting Information, Figure S10 for details). Consistent with findings from transient absorption, fluorescence emission from excitonic traps is much enhanced from 3D to 2D. The $\rho_{\text{trap}}/\rho_{\text{BG}}$ ratio from the 2D sample is 5 \times and 20 \times of that from the 3D sample at 78 and 100 K, respectively. For each sample, the $\rho_{\text{trap}}/\rho_{\text{BG}}$ ratio decreases with increasing temperature, indicating that the trapped excitons can be thermally activated into band gap excitons. Plot of $\ln(\rho_{\text{trap}}/\rho_{\text{BG}})$ vs $1/T$ do not show linear relationships (Supporting Information, Figure S11), suggesting that the energetic gaps between trap states and band gap excitons are not constants, as expected from the broad energetic distributions of trap states. The varying slope in $\ln(\rho_{\text{trap}}/\rho_{\text{BG}})$ vs $1/T$ gives phenomenological free energy difference between band-edge excitons and trapped excitons of -5 to -54 meV and -28 to -102 meV for 2D ($n = 1$) and 3D (from PbI_2) perovskites, respectively; the absolute values of these numbers are smaller than those of the mean trap energies (see next section), as expected from the sequential thermal activation within the trap state manifold and, finally, to the band gap excitons. A quantitative understanding of these temperature dependences would require a detailed understanding of the interconversion among the broad distribution of trap states, the thermal activation of the trap states into band gap excitons, and competing radiative and nonradiative recombination rates from these states.⁴¹ Further experiments and modeling are underway to quantify the various rates.

The Surface/Interface Origin of Trap States: A Hypothesis. To understand the origins of trap states, we first summarize our findings presented above: (1) photo-emission measurements revealed similar hole traps on the exposed surfaces of 3D perovskites from both PbCl_2 and PbI_2 ; and (2) the density of excitonic traps is much increased when we go from 3D perovskites (from PbI_2) to 2D perovskites and, within the 2D family, as the relative surface area increases. This is reflected semiquantitatively in the relative amplitude of trap state bleaching to bandgap bleaching (γ): $\gamma = 0.045$ in 3D perovskite from PbI_2 , $\gamma = 0.077, 0.25$, and 0.30 for 2D perovskites with $n = 3, 2$, and 1 , respectively. On the basis of this correlation between interfacial area and the density of excitonic traps, we hypothesize that the trap states are localized

at the crystallite surfaces and interfaces where the bulk crystalline symmetry is broken.

We point out two key features of the excitonic traps. First, both an electron and a hole can be trapped, resulting in an excitonic trap possessing weak transition dipole in absorption or emission. Second, the energetic distribution of traps is very broad and located within ~ 100 – 400 meV below the band gap exciton in each case. For the three QW samples, Figure 3 gives mean trap energies (referenced to E_{OG}) of $\langle E_{\text{trap}} \rangle = -0.33 \pm 0.12$, -0.17 ± 0.05 , and -0.17 ± 0.07 eV for $n = 1, 2$, and 3 respectively. Similar analysis from low-temperature fluorescence spectra in Figure 4 yields mean trap energies of $\langle E_{\text{trap}} \rangle = -0.38 \pm 0.15$ eV for the 2D ($n = 1$) sample and $\langle E_{\text{trap}} \rangle = -0.12 \pm 0.05$ eV for the 3D sample. Both the broadness of the trap energies and the relative, not absolute, energetic positions of excitonic traps referenced to different optical gaps suggest that the excitonic traps unlikely originate from common chemical defects,^{33,34} but rather from the self-trapping of band-edge excitons.⁴² For a specific chemical defect, the trap state energy is expected to be well-defined, which is not the case here.

The formation of a self-trapped exciton results from exciton–phonon interaction, which is predicted to critically depend on the dimensionality of a crystalline system.⁴² Lowering the dimension of a system lowers the deformation energy, thus making self-trapping easier.⁴² In the limit of one-dimensional perovskites, all excitons are self-trapped with extraordinarily large Stokes shifts of ~ 1 eV.^{43–45} There is usually a large potential barrier for exciton self-trapping in 3D, while the 2D system is a marginal case and possesses lower activation energy for self-trapping.⁴² Our observations presented above are consistent with this general principle. Strong electron–phonon coupling has been invoked to account for below-gap³⁰ and white light emission⁴⁶ in 2D layered perovskites. This coupling has also been invoked to account for the homogeneous emission line broadening in 3D perovskites.⁴⁷ For a 3D perovskite crystallite, the terminal methylammonium cations are freer to move than their counter parts in the bulk, leading to easier self-trapping on the surface, particularly when the surface termination deviates from the low-index crystalline planes.³⁸ The self-trapped excitons on the surface can be formed from direct optical excitation due to the none-zero oscillator strength or from the dynamic relaxation of the band-edge Mott–Wannier exciton or carriers. At room temperature, the self-trapped excitons, with average trapping energy of $\langle E_{\text{trap}} \rangle = -0.12 \pm 0.05$ eV, can effectively equilibrate with band-edge excitons/carriers given the large entropic driving from a surface state to bulk states. This equilibrium explains that the self-trapped exciton possesses similar lifetime as the band-edge exciton/carriers, as seen in Figure 2D.

4. SUMMARY

The results presented here suggest an intrinsic origin of below-gap excitonic and carrier traps in lead iodide perovskites: the trap states can result from electron–phonon coupling at surfaces/interfaces of crystalline perovskites. In such an interface/phonon interpretation of trap states, the surface of a 3D perovskite film can be considered “entirely” as source for the self-trapped charge (i.e., polaron) or self-trapped exciton. Charge carrier trapping at interfaces between the perovskite thin film and electron or hole transporting layers is believed to result in faster recombination than that in bulk film²⁵ and these interfacial traps have also been implicated for anomalous hysteresis in current/voltage curves in perovskite solar cells.²³

Optical measurements revealed a much higher density of excitonic traps in the bulk of the perovskite thin film grown in the absence of chloride than that with chloride, explaining the higher solar cell efficiency in the latter. A comparison to recent structural characterization of perovskite thin films from these two sample preparations suggests that the trap states are associated with interfaces of crystallites lacking well-defined facets of low Miller indices.²⁷ In addition to growth of sufficiently large crystallites with low Miller indices, we may envision passivation of surfaces/interfaces traps with organic molecules³⁴ or a rigid termination layer, such as PbI_2 .⁴⁸ How to manage or control surface and interface trapping may be key to the stabilization of perovskite based solar cells.

■ ASSOCIATED CONTENT

Supporting Information

Materials and methods, additional results, and references. This material is available free of charge via the Internet at <http://pubs.acs.org>.

■ AUTHOR INFORMATION

Corresponding Author

xyzhu@columbia.edu

Author Contributions

[†]X.W., T.T., D.N., and H.Z. contributed equally.

Notes

The authors declare no competing financial interest.

■ ACKNOWLEDGMENTS

The preparation of vapor-deposited perovskite samples, UPS measurements, and fluorescence measurements were supported by the US Department of Energy under Grant No. ER46980. The transient absorption measurements were supported by the US National Science Foundation under Grant Number DMR-1125845. Research carried out in part at the Center for Functional Nanomaterials, Brookhaven National Laboratory, which is supported by the U.S. Department of Energy, Office of Basic Energy Sciences, under Contract Number DE-AC02-98CH10886. D. N. acknowledges support by the Deutsche Forschungsgemeinschaft (DFG Forschungsspendium). We thank Matthew Y. Sfeir for technical help with transient absorption measurements, Joshua Choi for providing solution based 3D perovskite samples, and Prakriti Joshi for help with vapor deposition of 3D perovskite samples.

■ REFERENCES

- (1) Kojima, A.; Teshima, K.; Shirai, Y.; Miyasaka, T. *J. Am. Chem. Soc.* **2009**, *131*, 6050.
- (2) Im, J.-H.; Lee, C.-R.; Lee, J.-W.; Park, S.-W.; Park, N.-G. *Nanoscale* **2011**, *3*, 4088.
- (3) Chung, I.; Lee, B.; He, J.; Chang, R. P. H.; Kanatzidis, M. G. *Nature* **2012**, *485*, 486.
- (4) Kim, H.-S.; Lee, C.-R.; Im, J.-H.; Lee, K.-B.; Moehl, T.; Marchioro, A.; Moon, S.-J.; Humphry-Baker, R.; Yum, J.-H.; Moser, J. E.; Grätzel, M.; Park, N.-G. *Sci. Rep.* **2012**, *2*, 591.
- (5) Lee, M. M.; Teuscher, J.; Miyasaka, T.; Murakami, T. N.; Snaith, H. J. *Science* **2012**, *338*, 643.
- (6) Etgar, L.; Gao, P.; Xue, Z.; Peng, Q.; Chandiran, A. K.; Liu, B.; Nazeeruddin, M. K.; Grätzel, M. *J. Am. Chem. Soc.* **2012**, *134*, 17396.
- (7) Liu, M.; Johnston, M. B.; Snaith, H. J. *Nature* **2013**, *501*, 395.
- (8) Burschka, J.; Pellet, N.; Moon, S.-J.; Humphry-Baker, R.; Gao, P.; Nazeeruddin, M. K.; Grätzel, M. *Nature* **2013**, *499*, 316.
- (9) Green, M. A.; Ho-Baillie, A.; Snaith, H. J. *Nat. Photonics* **2014**, *8*, 506.

- (10) Stranks, S. D.; Eperon, G. E.; Grancini, G.; Menelaou, C.; Alcocer, M. J. P.; Leijtens, T.; Herz, L. M.; Petrozza, A.; Snaith, H. J. *Science* **2013**, *342*, 341.
- (11) Xing, G.; Mathews, N.; Sun, S.; Lim, S. S.; Lam, Y. M.; Grätzel, M.; Mhaisalkar, S.; Sum, T. C. *Science* **2013**, *342*, 344.
- (12) Wehrenfennig, C.; Eperon, G. E.; Johnston, M. B.; Snaith, H. J.; Herz, L. M. *Adv. Mater.* **2013**, *26*, 1584.
- (13) Marchioro, A.; Teuscher, J.; Friedrich, D.; Kunst, M.; van de Krol, R.; Moehl, T.; Grätzel, M.; Moser, J.-E. *Nat. Photonics* **2014**, *8*, 250.
- (14) D'Innocenzo, V.; Grancini, G.; Alcocer, M. J. P.; Kandada, A. R. S.; Stranks, S. D.; Lee, M. M.; Lanzani, G.; Snaith, H. J.; Petrozza, A. *Nat. Commun.* **2014**, *5*, 3586.
- (15) Mei, A.; Li, X.; Liu, L.; Ku, Z.; Liu, T.; Rong, Y.; Xu, M.; Hu, M.; Chen, J.; Yang, Y.; Grätzel, M.; Han, H. *Science* **2014**, *345*, 295.
- (16) Hao, F.; Stoumpos, C. C.; Cao, D. H.; Chang, R. P. H.; Kanatzidis, M. G. *Nat. Photonics* **2014**, *8*, 489.
- (17) Zhou, H.; Chen, Q.; Li, G.; Luo, S.; Song, T. -b.; Duan, H.-S.; Hong, Z.; You, J.; Liu, Y.; Yang, Y. *Science* **2014**, *345*, 542.
- (18) Mitzi, D. B. In *Progress in Inorganic Chemistry*; John Wiley & Sons, Inc.: New York, 2007; pp 1–121.
- (19) Ishihara, T.; Takahashi, J.; Goto, T. *Phys. Rev. B: Condens. Matter Mater. Phys.* **1990**, *42*, 11099.
- (20) Tanaka, K.; Kondo, T. *Sci. Technol. Adv. Mater.* **2003**, *4*, 599.
- (21) Ponce, C. S.; Savenije, T. J.; Abdellah, M.; Zheng, K.; Yartsev, A.; Pascher, T.; Harlang, T.; Chabera, P.; Pullerits, T.; Stepanov, A.; Wolf, J.-P.; Sundström, V. *J. Am. Chem. Soc.* **2014**, *136*, 5189.
- (22) Manser, J. S.; Kamat, P. V. *Nat. Photonics* **2014**, *8*, 737.
- (23) Snaith, H. J.; Abate, A.; Ball, J. M.; Eperon, G. E.; Leijtens, T.; Noel, N. K.; Stranks, S. D.; Wang, J. T.-W.; Wojciechowski, K.; Zhang, W. *J. Phys. Chem. Lett.* **2014**, *5*, 1511.
- (24) Leijtens, T.; Stranks, S. D.; Eperon, G. E.; Lindblad, R.; Johansson, E. M. J.; McPherson, I. J.; Rensmo, H.; Ball, J. M.; Lee, M. M.; Snaith, H. J. *ACS Nano* **2014**, *8*, 7147.
- (25) Wang, L.; McCleese, C.; Kovalsky, A.; Zhao, Y.; Burda, C. *J. Am. Chem. Soc.* **2014**, *136*, 12205.
- (26) Grätzel, M. *Nat. Mater.* **2014**, *13*, 838.
- (27) Dar, M. I.; Arora, N.; Gao, P.; Ahmad, S.; Grätzel, M.; Nazeeruddin, M. K. *Nano Lett.* **2014**, *14*, 6991.
- (28) Colella, S.; Mosconi, E.; Fedeli, P.; Listorti, A.; Gazza, F.; Orlandi, F.; Ferro, P.; Besagni, T.; Rizzo, A.; Calestani, G.; Gigli, G.; De Angelis, F.; Mosca, R. *Chem. Mater.* **2013**, *25*, 4613.
- (29) Zhao, Y.; Zhu, K. J. *Phys. Chem. C* **2014**, *118*, 9412.
- (30) Gauthron, K.; Lauret, J.-S.; Doyennette, L.; Lanty, G.; Al Choueiry, A.; Zhang, S. J.; Brehier, A.; Largeau, L.; Mauguin, O.; Bloch, J.; Deleporte, E. *Opt. Express* **2010**, *18*, 5912.
- (31) Tanaka, K.; Takahashi, T.; Ban, T.; Kondo, T.; Uchida, K.; Miura, N. *Solid State Commun.* **2003**, *127*, 619.
- (32) Yin, W.-J.; Shi, T.; Yan, Y. *Appl. Phys. Lett.* **2014**, *104*, 063903.
- (33) Kim, J.; Lee, S.-H.; Lee, J. H.; Hong, K.-H. *J. Phys. Chem. Lett.* **2014**, *5*, 1312.
- (34) Noel, N. K.; Abate, A.; Stranks, S. D.; Parrott, E.; Burlakov, V.; Goriely, A.; Snaith, H. J. *ACS Nano* **2014**, *8*, 9815.
- (35) Schulz, P.; Edri, E.; Kirmayer, S.; Hodes, G.; Cahen, D.; Kahn, A. *Energy Environ. Sci.* **2014**, *7*, 1377.
- (36) Williams, S. T.; Zuo, F.; Chueh, C.-C.; Liao, C.-Y.; Liang, P.-W.; Jen, A. K.-Y. *ACS Nano* **2014**, *8*, 10640.
- (37) Edri, E.; Kirmayer, S.; Henning, A.; Mukhopadhyay, S.; Gartsman, K.; Rosenwaks, Y.; Hodes, G.; Cahen, D. *Nano Lett.* **2014**, *14*, 1000.
- (38) Haruyama, J.; Sodeyama, K.; Han, L.; Tateyama, Y. *J. Phys. Chem. Lett.* **2014**, *5*, 2903.
- (39) Kawamura, Y.; Mashiyama, H.; Hasebe, K. *J. Phys. Soc. Jpn.* **2002**, *71*, 1694.
- (40) Wehrenfennig, C.; Liu, M.; Snaith, H. J.; Johnston, M. B.; Herz, L. M. *APL Mater.* **2014**, *2*, 081513.
- (41) Stranks, S. D.; Burlakov, V. M.; Leijtens, T.; Ball, J. M.; Goriely, A.; Snaith, H. J. *Phys. Rev. Appl.* **2014**, *2*, 034007.
- (42) Song, K. S.; Williams, R. T. *Self-Trapped Excitons*; Springer Series in Solid-State Sciences; Springer: Berlin, 1993; Vol. 105.
- (43) Trigui, A.; Abid, H.; Mlayah, A.; Abid, Y. *Synth. Met.* **2012**, *162*, 1731.
- (44) Tanaka, K.; Ozawa, R.; Umebayashi, T.; Asai, K.; Ema, K.; Kondo, T. *Phys. E (Amsterdam, Neth.)* **2005**, *25*, 378.
- (45) Tanino, H.; Rühle, W.; Takahashi, K. *Phys. Rev. B: Condens. Matter Mater. Phys.* **1988**, *38*, 12716.
- (46) Dohner, E. R.; Jaffe, A.; Bradshaw, L. R.; Karunadasa, H. I. *J. Am. Chem. Soc.* **2014**, *136*, 13154.
- (47) Wehrenfennig, C.; Liu, M.; Snaith, H. J.; Johnston, M. B.; Herz, L. M. *J. Phys. Chem. Lett.* **2014**, *5*, 1300.
- (48) Chen, Q.; Zhou, H.; Song, T.-B.; Luo, S.; Hong, Z.; Duan, H.-S.; Dou, L.; Liu, Y.; Yang, Y. *Nano Lett.* **2014**, *14*, 4158.